Journal of Materials Processing Tech. 294 (2021) 117139

Contents lists available at ScienceDirect

Journal of Materials Processing Tech.

journal homepage: www.elsevier.com/locate/jmatprotec

Directed energy deposition build process control effects on microstructure and tensile failure behaviour

Eddie Tan Zhi'En [a,b,*], John Hock Lye Pang [a], Jacek Kaminski [b]

[a] Nanyang Technological University, School of Mechanical and Aerospace Engineering, 50 Nanyang Avenue, Singapore, 639798, Singapore
[b] Advanced Remanufacturing and Technology Centre, 3 CleanTech Loop, CleanTech Two, Singapore, 637143, Singapore

ARTICLE INFO

Associate Editor: Marion Merklein

Keywords:
Directed energy deposition
Hall-Petch
Microstructure
Stainless steel 316L
Tensile properties

ABSTRACT

An investigation on the effects of additive manufacturing build strategy raster scan patterns on process control, microstructure, and mechanical properties is reported in this study. Although the effects of build orientation on the properties of AM-built components are well understood, the effects of build strategy on material and mechanical properties have yet to be explored in detail. This study looks into the effects of directed energy deposition build strategy on the materials and mechanical properties of Stainless Steel 316 L show interesting build strategy trends. Three different directed energy deposition raster scan strategies, namely: short unidirectional, bidirectional, and long unidirectional raster scan deposition patterns were evaluated. Tensile tests were conducted to characterise the variability in mechanical properties of the directed energy deposition built specimens compared to bar stock material properties. The results show different anisotropic properties for each build strategy. The highest tensile strength, yield stress, and fracture strain were observed for the long unidirectional raster scan build strategy, followed by the bidirectional and short unidirectional raster scan build strategies.

1. Introduction

Additive Manufacturing (AM) has gained significant interest in the recent years as a means for processing metallic materials for a wide variety of applications. Laser metal deposition (LMD) is a directed energy deposition (DED) technology that fabricates components additively in a layer-by-layer deposition sequence. The AM deposition head feeds metal powder via a coaxial nozzle according to scan path programs generated from either computer-aided manufacturing models or user-defined codes and undergoes a melt-solidification sequence using a high power laser beam. LMD can be used to fabricate a wide range of components including functionally graded materials (FGM) and functional components applicable in numerous functional applications. Su et al. (2020) demonstrated the use of LMD techniques to produce Stainless Steel 316 L and Inconel 718 FGM and investigated the effects of the composition gradient on microstructural and mechanical properties. Huang et al. (2019) showed that by controlling thermal and solidification parameters of LMD, the quality of LMD built Stainless Steel 316 L and Inconel 625 parts can be controlled.

The thermal history of AM-built parts is highly complex due to the numerous combinations of build parameters and their interactions. The thermal cycling that occurs during the layer-by-layer deposition process results in a microstructural evolution that changes rapidly throughout the AM process. For example, it has been generally established that different degrees of anisotropic characteristics can arise by varying the build orientation of the AM components. Zhang et al. (2014) demonstrated that the layer-based principle of AM techniques holds restrictions like the anisotropy of mechanical and structural properties and showed that tensile tests and SEM morphologies of specimen fractures built in differing orientations exhibit anisotropic properties. Due to the complexity of AM processes, many parameters, not limited to the build orientation, play a crucial role in influencing the thermal history. Amine et al. (2014) found that the deposition scan speed and laser power have a significant effect on the microstructural growth, and that the thermal history of LMD can be described as a series of reheating cycles, or discrete pulses of heat. If the thermal history that arises from the orientation of the component with respect to the deposition plays an important role in the unique microstructural growth that gives rise to anisotropy, it is crucial to investigate if changes to the deposition track patterns within each layer have a tangible effect on the mechanical properties of the part. With the development various types of deposition scan patterns in AM, the thermal cycling that occurs between deposition

* Corresponding author.
E-mail address: eddie.tanze@ntu.edu.sg (E. Tan Zhi'En).

https://doi.org/10.1016/j.jmatprotec.2021.117139
Received 22 November 2020; Received in revised form 15 February 2021; Accepted 2 March 2021
Available online 10 March 2021
0924-0136/

tracks become a point of interest, as the thermal history compounds in complexity from pattern to pattern.

Although multiple modelling studies currently exist, showing a clear relationship between build strategy and the thermal history of LMD built components, little work has been done to control the degree of variation in thermal gradient during the LMD process. For instance, Farahmand and Kovacevic (2014) developed a finite element model to calculate the thermal and stress components of single and multi-track LMD. Yu et al. (2011) demonstrated by finite element modelling simulation that various deposition patterns like raster, offset out, offset in, and fractal generates different temperature gradients. One approach to improving the quality of the LMD built component is by identifying the bounds of a process window that is predictive of the LMD quality that is desired. Shi et al. (2018) used statistical methods to optimise the process parameters of LMD applications and found that scan velocity and powder feed were crucial to controlling the thickness and dilution of the deposited metal. Erfanmanesh et al. (2017) likewise, used empirical-statistical methods to conduct a process optimization on LMD built parts and established a process window in order to acquire desired geometry and low-porosity LMD parts. Another approach to improve the quality of LMD built components is to employ in-situ control measures for the LMD process. Several process monitoring techniques exist using photodiodes and pyrometers, melt pool height triangulations, and thermal imaging methods. Tyralla and Seefeld (2020) integrated a two-channel pyrometer camera into the LMD head, enabling in-situ evaluation of several thermal indicator values. Donadello et al. (2018) presented an in-situ deposition height monitoring technique using triangulation methods with a probe laser mounted coaxially through the LMD nozzle and a coaxial camera that measures the probe spot by converting relative height values. Kisielewicz et al. (2018) demonstrated the use of spectroscopy techniques of DED built parts by measuring the intensity of continuum radiation as a relation to laser power input parameter. Forien et al. (2020) combined the use of in-situ high speed pyrometry and melt pool imaging to identify conduction and keyhole mode laser processing conditions that lead to defects caused by keyhole instability. Although many types of in-situ process monitoring techniques currently exist in the field of AM, little work has been done on the utilisation of these methods to control the effects of build strategy on the variations in thermal history, and to evaluate if any anisotropic properties persist through the process control.

The motivation of this research is to characterise the effects of build strategy on LMD built parts and quantify its influence on the process control and anisotropy in mechanical properties that arises from its microstructure. Although the effects of build orientation have been studied extensively by researchers, little empirical work has been done in investigating other sources of anisotropy like the raster scan build strategy and its effects on the process control, material, and mechanical characteristics in LMD processes. This study explores the extent of an additional source of anisotropy and measure its impact on the behaviour of the LMD build. An illustration of the distinction in LMD build methodology between existing studies on build orientation and this study's work on build strategy is illustrated in Fig. 1. Tensile specimens were extracted from build-up specimens in order to evaluate the build strategy's effect on its mechanical anisotropy. Microstructural studies were conducted in order to observe the grain growth differences between each build strategy and correlate the grain characteristics with the anisotropy from the tensile tests.

2. Methodology

2.1. Laser metal deposition process

The DMG MORI LaserTec 65 3D machine was used to fabricate AM built LMD specimens from Stainless Steel 316 L powder feed using three different build strategies: long unidirectional, bidirectional, and short unidirectional raster scan deposition process. The LMD process used in this experiment is illustrated in a schematic diagram as shown in Fig. 2, where a diode laser is used as a laser source, and argon as the shielding gas. A laser power of 1300 W, laser spot diameter of 3 mm, powder deposition rate of 14 g/min, scanning speed of 1000 mm/min and deposition track overlap of 60 % was used. The metal powder was fed coaxially and melted by a diode laser to form a melt pool at the substrate. The deposition head moves with accordance to the defined build strategies' scan paths and builds the part layer by layer.

2.2. Powder material

The powder material used in the LMD process was Stainless Steel 316 L. The SS316 L powder feed is gas atomized spherical metallic granules prepared by Carpenter. A Scanning Electron Microscope (SEM) image of the powder material with a particle size range of 45 µm – 105 µm was taken using a Zeiss EVO HD 25, and is shown in Fig. 3. The LMD process

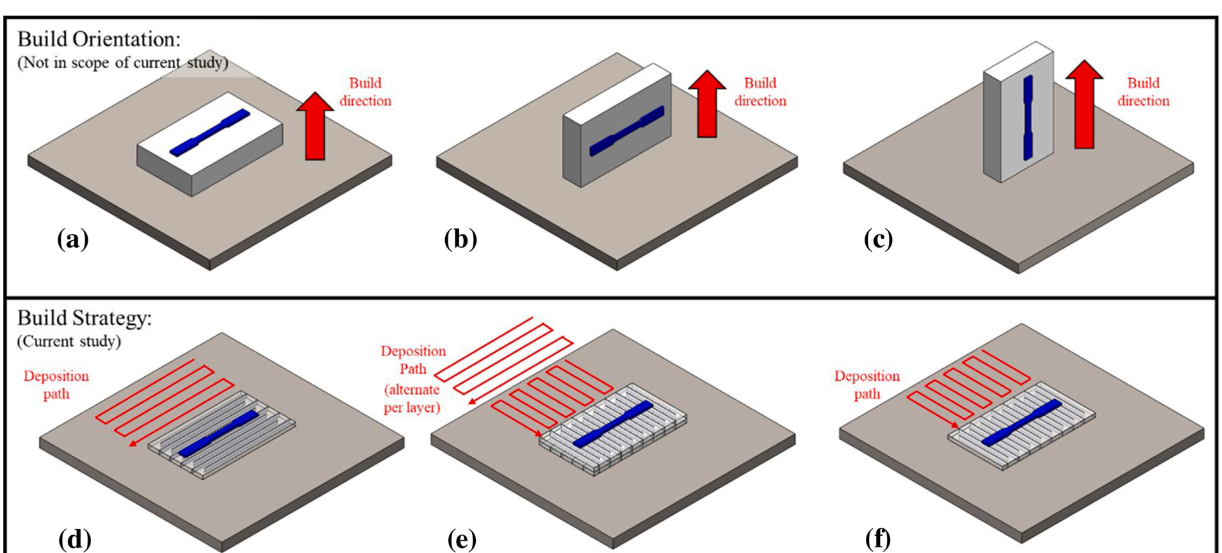

Fig. 1. Illustration of LMD build orientation types from existing studies on anisotropy (a) base build orientation, (b) longitudinal build orientation, (c) transverse build orientation, and illustration of LMD build strategy types from this study on alternative sources of anisotropy (d) long unidirectional build strategy, (e) bidirectional build strategy, (f) short unidirectional build strategy.

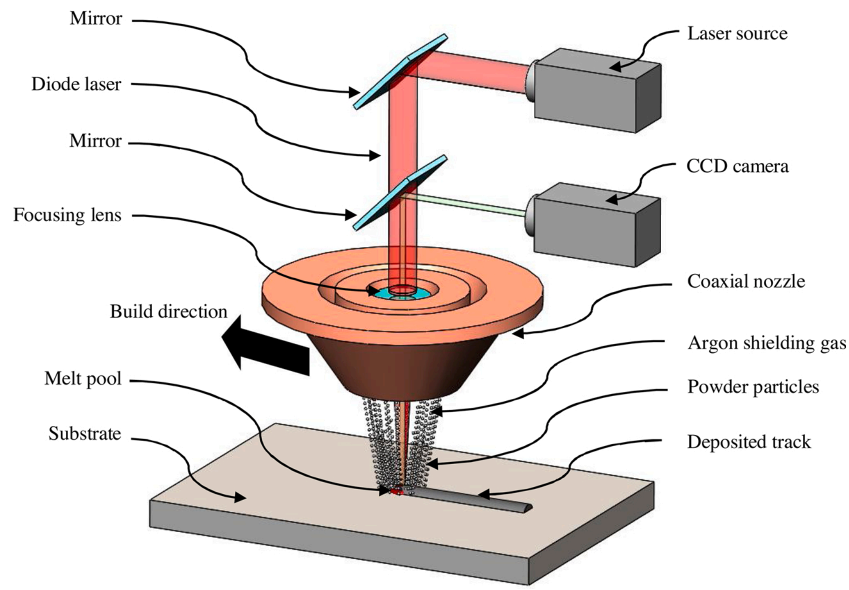

Fig. 2. LMD schematic diagram.

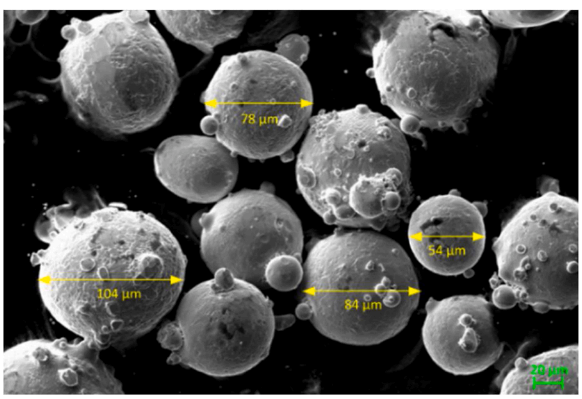

Fig. 3. SEM image of powder feed particles.

was fabricated on a mild steel base plate substrate of dimensions 250 mm × 250 mm × 9 mm. The chemical composition of the SS316 L powder feed is shown in Table 1.

2.3. LMD build specimens

Three specimens were fabricated for each build strategy type: long unidirectional, bidirectional, and short unidirectional raster scan. The long unidirectional raster scan build strategy employs a raster scan pattern that runs longitudinally, parallel to the long edge of the specimen. For unidirectional raster scan patterns, the deposition track overlap was set at 60 %. The short unidirectional raster scan build strategy's deposition method is similar to the long unidirectional raster scan build strategy, with the exception that the raster scan runs transversely, parallel to the short edge of the specimen. The bidirectional raster scan build strategy alternates between a longitudinal and transverse raster scan pattern between the deposited layers. For all build strategies, the scan path initiation point per layer is situated diagonally across from the previous layer's initiation point. The build strategy scan patterns as described are illustrated in Fig. 4. The dimensions of the block specimens produced by LMD are 206 mm long, 26 mm wide, and 9 mm thick. These dimensions were chosen based on an inclusion of a 3 mm overbuild at all sides to allow for tensile specimens to be extracted from the LMD block specimens. Tensile specimens dimensions of 60 mm long, 12.5 mm wide, 4 mm thick were selected with accordance to ASTM E8/E8M (ASTM, 2016a,b). To ensure that the LMD samples were built to specification and has the build volume required to extract tensile specimens, the dimensions of the LMD samples were verified using an articulated laser coordinate-measuring machine (CMM) as seen in Fig. 4.

Tensile specimens were subsequently extracted from each of the nine LMD built blocks using milling and grinding techniques. Stainless Steel 316 L specimens were also extracted from stock bar material from extrusion followed by cold rolling process, with accordance to ASTM A276/A276M-17, and was used as a point of reference for comparison with the specimens produced by LMD (ASTM, 2017). A total of twelve tensile specimens were fabricated, with three repetitions for the four experimental test specimen conditions shown in Fig. 5.

2.4. Experimental procedure

A visual sensory system, in the form of a CCD camera, was used to monitor the melt pool during the LMD process. The CCD camera's capture view was directed perpendicular to the substrate toward the deposition site. Video capture of the melt pool was taken and the melt pool characteristics, including the melt pool temperature, melt pool size, were measured and recorded, and the laser power was adjusted in real-time with accordance to the in-situ control parameters. A temperature melt threshold of 1560 °C, laser power boundary of 700 W (minimum) and 1800 W (maximum), maximum laser power ramp of 50 W/sec, and a sampling rate of 10 samples per second were used as input for the in-situ process control parameters.

Tensile tests were conducted on the specimens using a Shimadzu Tensile Tester equipped with a 50 kN load cell with a strain rate of 0.05 /min, and a digital video extensometer was used for strain

Table 1
Nominal chemical composition of SS316 L powder feed (wt.%).

Material	C	Mn	P	S	Si	Cr	Ni	Mo	Fe
SS316 L	0.03	2.00	0.045	0.03	1.00	16.00–18.00	10.00–14.00	2.00–3.00	Bal.

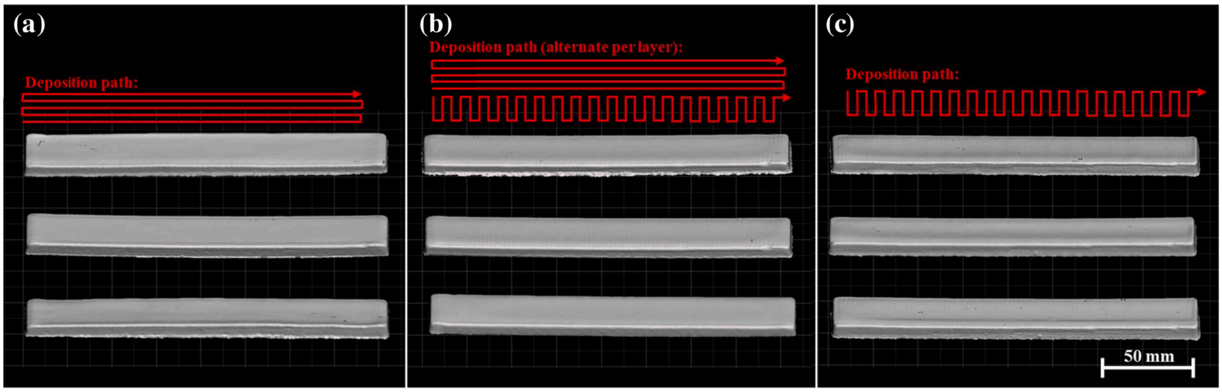

Fig. 4. Laser CMM scans of LMD specimens built using (a) long unidirectional raster scan, (b) bidirectional raster scan, and (c) short raster scan build strategies.

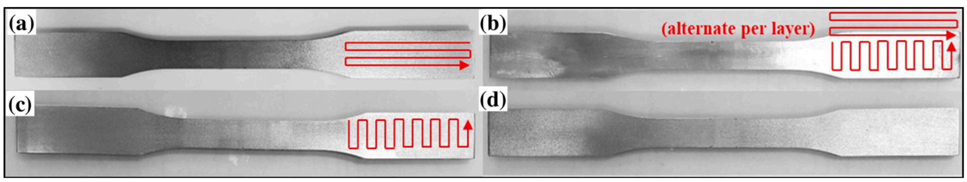

Fig. 5. Tensile specimens for four experimental test specimen conditions (a) long unidirectional raster scan, (b) bidirectional raster scan, (c) short unidirectional raster scan and (d) stock.

measurement. After the tensile tests, the specimens' fracture surface topologies were scanned using the Zeiss Smart Zoom 5, via a 3D depth-of-focus reconstruction method using 34 times magnification with a 30 μm resolution. The specimens were sectioned at the grip length area, 30 mm away from the edge, and the sectioned surface was etched in a solution of 5% vol. nitric acid, 5% vol. hydrochloric acid, and 90 % vol. ethanol. The section location and measurement surface are illustrated in Fig. 6.

Micrographs of the microstructure were captured using a Zeiss Light Microscope and characterised using Fiji software. To measure the grain size, the ASTM E112−13's Abrams Three-Circle procedure was used due to its suitability for measuring non-equiaxed grain structures, typically observed for LMD-built materials (ASTM, 2014). The results were then plotted against the yield strength from the tensile tests and correlated via the Hall-Petch relationship. The Hall-Petch relationship describes the correlation between microstructural grain size and yield stresses via the following equation (Kashyap and Tangri, 1995; Hansen, 2004):

$$\sigma_y = \sigma_0 + \frac{k}{\sqrt{d}} \tag{1}$$

where σ_y is yield strength, σ_0 is a material constant that governs the stresses for grain dislocation movement, k is the Hall-Petch slope coefficient, and d is the grain size. The Hall-Petch relationship generally describes how the yield strength of the material increases with decreasing microstructural grain size.

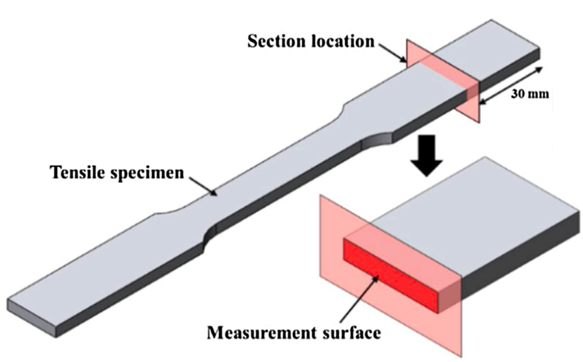

Fig. 6. Section location on tensile specimen for micrograph and micro-indentation measurements.

SEM images were captured using Zeiss EVO SEM equipment and analysed with Inca software. Aztec software was further used to conduct Energy-dispersive X-ray spectroscopy (EDX) analysis. SEM was set at Backscatter Electron (BSE) mode, 300 times magnification, 9 mm working distance and an Extra High Tension (EHT) voltage level of 15 kV.

Subsequently, micrographs of the deposition track body and fusion zones were captured using the Zeiss Light Microscope. Vickers micro hardness tests were conducted with accordance to ASTM E384−17 using an Innova Test Falcon 500 micro hardness tester (ASTM, 2016a,b). A micro-indentation load of 500 g and a 15 s dwell time were used at fusion zones and deposition track body locations.

3. Results and discussion

3.1. Process monitoring

Melt pool characteristics were measured and recorded during the LMD process. Three individual melt pool image captures taken in 0.5 s intervals were modelled in a 3D heat map shown in Fig. 7. The heat map shows a distinctively steep thermal gradient toward the leading edge of the melt pool, and a more gradual thermal gradient toward the rear edge of the melt pool. This observation in the heat mapping is a result of the laser source's gaussian energy distribution that can be expressed using the double ellipsoid volumetric source heat input model (Goldak, Chakravarti et al. 1984). The model describes the heat source's power distribution as an expression of two ellipsoidal quadrants, where the front quadrant is steeper than the rear quadrant.

From each sample's heat mapping, the melt pool size, melt pool temperature characteristics were measured and recorded. The process monitoring data was subsequently modelled respective to their XYZ coordinates and the laser power input as shown in Figs. 8–10. The mean melt pool temperature, melt pool size, and laser power input per deposition layer during the LMD process were graphed in Fig. 11. A high

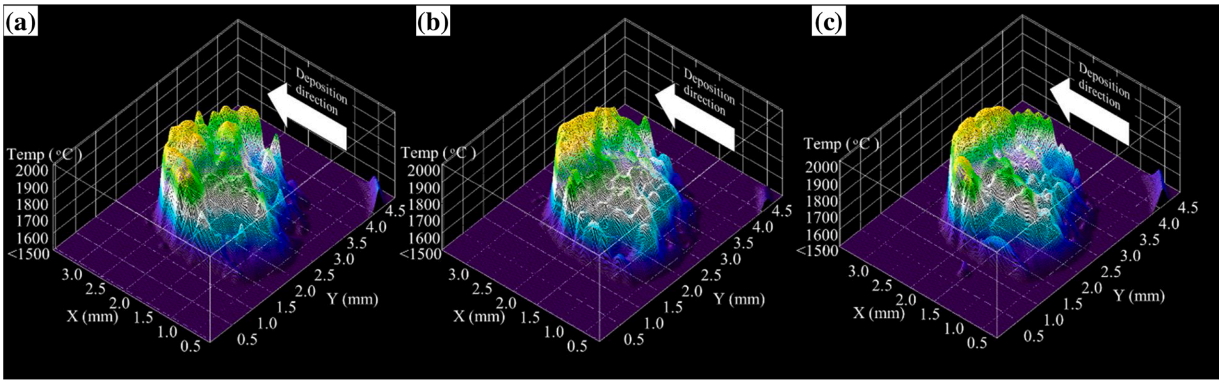

Fig. 7. 3D heat map model taken at LMD process time (a) 0.0 s, (b) 0.5 s, and (c) 1.0 s.

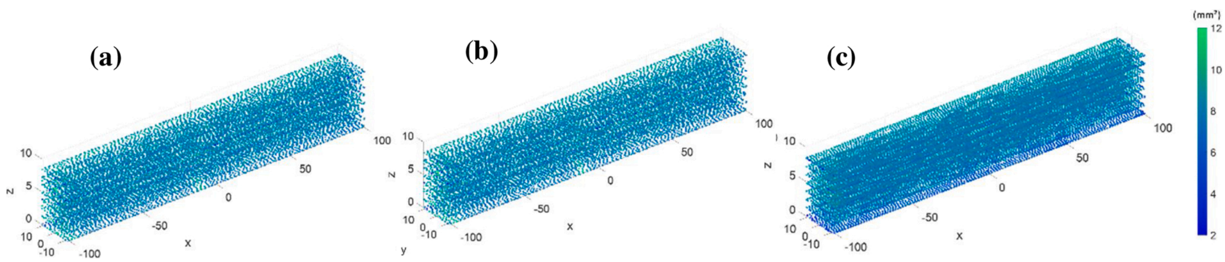

Fig. 8. LMD melt pool temperature process monitoring plot for (a) long unidirectional raster scan, (b) bidirectional raster scan, (c) short unidirectional raster scan.

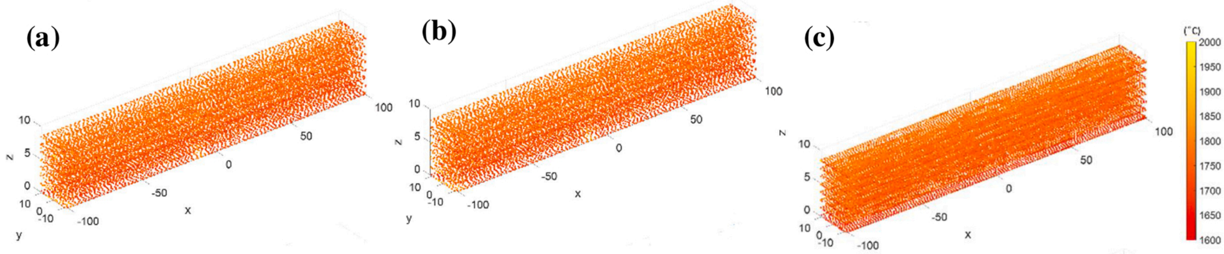

Fig. 9. LMD melt pool size process monitoring plot for (a) long unidirectional raster scan, (b) bidirectional raster scan, (c) short unidirectional raster scan.

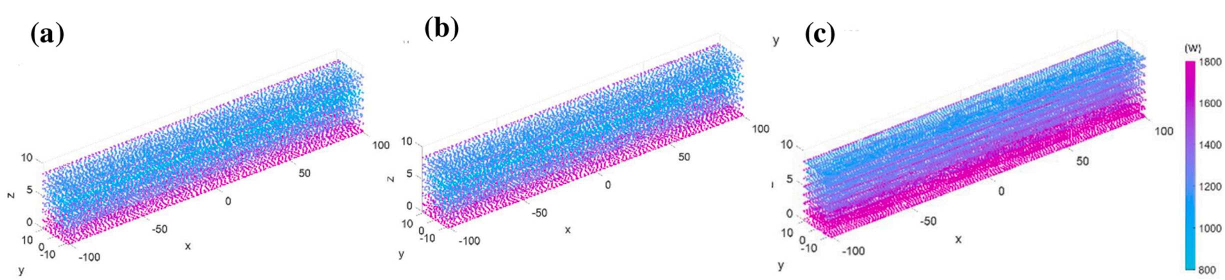

Fig. 10. LMD laser power input plot for (a) long unidirectional raster scan, (b) bidirectional raster scan, (c) short unidirectional raster scan.

degree of melt pool homogeneity was achieved during LMD process as a result of the in-situ adjustment of the laser power input as seen in Figs. 8 and 9. The mean laser power input across the LMD build for each condition was 1440 ± 45 W for the long unidirectional raster scan condition, 1304 ± 55 W for the bidirectional raster scan condition, and 1330 ± 77 W for the short unidirectional raster scan condition. To maintain a high degree of melt pool homogeneity, the laser power regulation for each condition varies widely, with the long unidirectional raster scan condition requiring approximately 8–10 % more energy input than the other two conditions.

The first deposition layer exhibited a lower melt pool temperature and smaller melt pool size due to the initial thermal conditions of the LMD process. The substrate's temperature at the point of the LMD initiation is cooler and hence requires a higher laser power input to achieve the necessary energy required to melt the deposited powder particles in the first deposition layer as seen in Fig. 11 (c). Beyond the first deposition layer, the heat energy and dissipation reaches a quasi-equilibrium state that results in a consistent mean melt pool temperature and melt pool size as seen in Fig. 11 (a) and (b). Each new deposition layer's initiation point is located diagonally across the previous

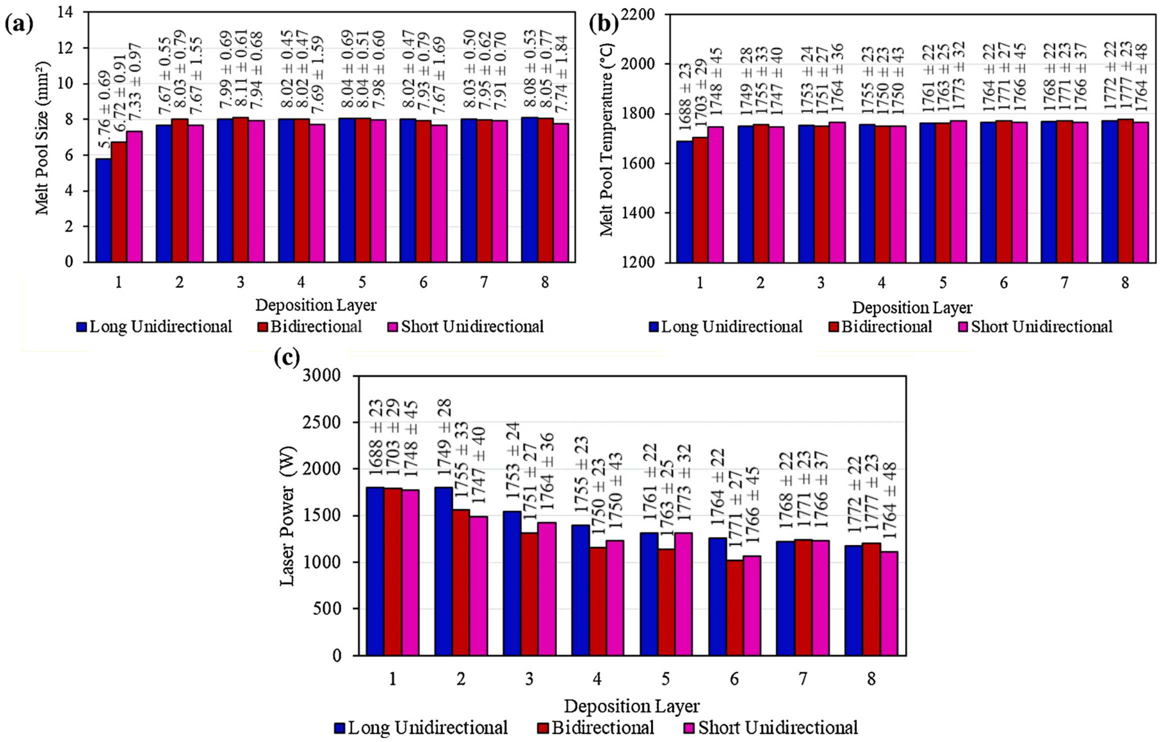

Fig. 11. LMD process monitoring mean data per deposition layer for (a) melt pool size, (b) melt pool temperature and (c) laser power input.

layer's initiation point. During the deposition head's translation to the new initiation point for the next layer, the previously deposited layer undergoes a significant cooling effect that necessitates a higher laser power input to achieve the target energy density. Furthermore, as more layers are deposited, lower laser power input is required for the LMD process due to the thermal energy build-up within the component body, that acts as a pre-heating element for each new layer that is deposited as seen in the decreasing laser power input reading from layer to layer in Fig. 11 (c). The long unidirectional raster scan's pattern that runs longitudinally across the long edge of the LMD block that produces a longer interval from one raster deposition path to the next, compared to the short unidirectional raster scan. The longer interval allows the area adjacent to the deposition area to cool down significantly before the subsequent deposition path in the raster pattern is produced. Hence, a higher energy density in the laser input is required to compensate for this cooling effect that results in a higher laser input for the long

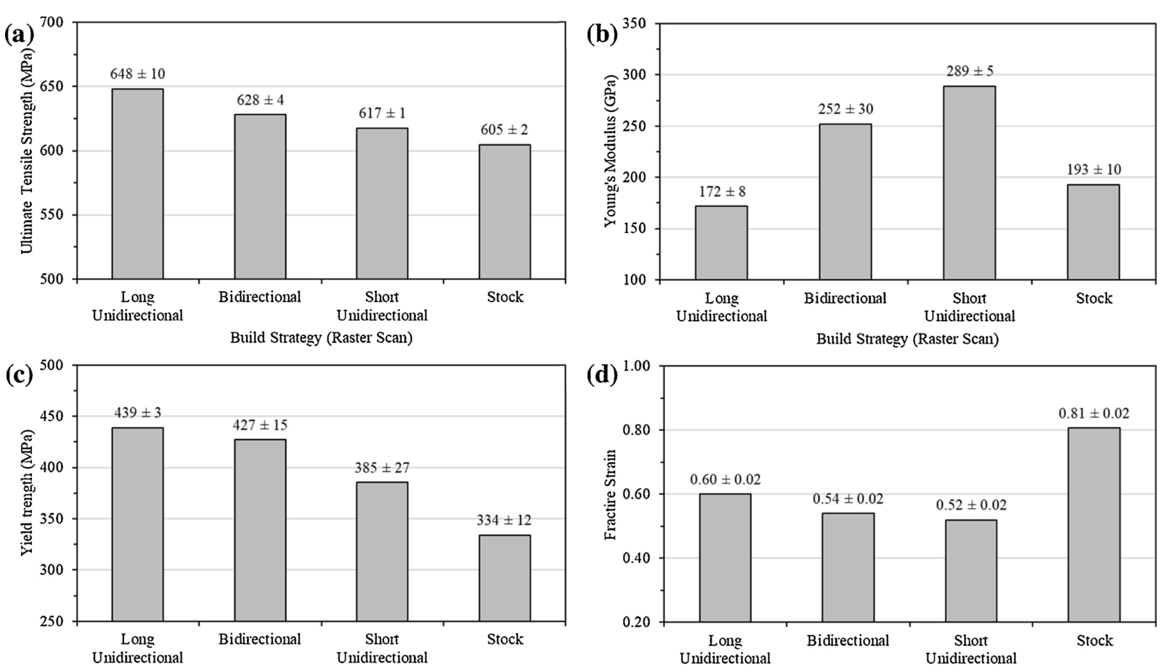

Fig. 12. Tensile test results for long unidirectional, bidirectional, short unidirectional raster scan build strategies and stock experiment conditions' (a) UTS, (b) Young's modulus, (c) yield strength, (d) fracture strain.

unidirectional raster scan build strategy than the other build strategies as seem in Fig. 11 (c).

3.2. Tensile test

Tensile test results for each experimental test specimen condition's ultimate tensile strength (UTS), Young's modulus, yield strength, and fracture strain, were measured and graphed in Fig. 12. Three samples were tested for each build strategy condition and their mean results are displayed.

The stock material specimens exhibit a lower UTS and yield strength, and a higher fracture strain than the LMD specimens. The long unidirectional raster scan build strategy exhibited the highest UTS, yield strength, and fracture strain among the LMD specimens, followed by the bidirectional and short unidirectional raster scan build strategies respectively, and the reverse trend is true for the Young's modulus result. The tensile test results indicate that there is an anisotropic tensile effect between the different build strategies.

3.3. Microstructure analysis

Microstructure images for the long unidirectional, bidirectional, short unidirectional raster scan build strategies and stock bar specimens are shown in Fig. 13. The section surface subjected to the microscope measurement for each sample is illustrated in Fig. 6.

The mean grain size for each build strategy specimen type condition were taken from the micrograph images as seen in Fig. 13 and compiled in Table 2. To measure these grain characteristics, the Abrams three-circle procedure was used to derive the mean grain size. The mean grain size for each condition were subsequently plotted against the experimental yield strength results in a Hall-Petch plot as shown in Fig. 14. From the Hall-Petch plot, a best fit linear trendline was applied to derive the σ_0 constant and k coefficients and were found to be 212 MPa and 722 MPa respectively.

From Fig. 13 (d), the stock specimens exhibited large near-equiaxed austenitic grain structures. The LMD specimens' microstructure observed from Fig. 13 (a), (b), and (c) from Table 2 show needle-like, acicular crystallite phase. The acicular crystals are observably

Table 2
Grain size data used in Hall-Petch relationship and plot.

	Grain size measurement	Hall-Petch model parameters	
	Mean Grain Size, d (μm)	$d^{-0.5}$ ($\mu m^{-0.5}$)	Yield Strength, σ_y (MPa)
1 Long Unidirectional	9.7 ± 0.9	0.32	439 ± 3
2 Bidirectional	13.0 ± 0.8	0.28	427 ± 15
3 Short Unidirectional	15.7 ± 1.2	0.25	385 ± 27

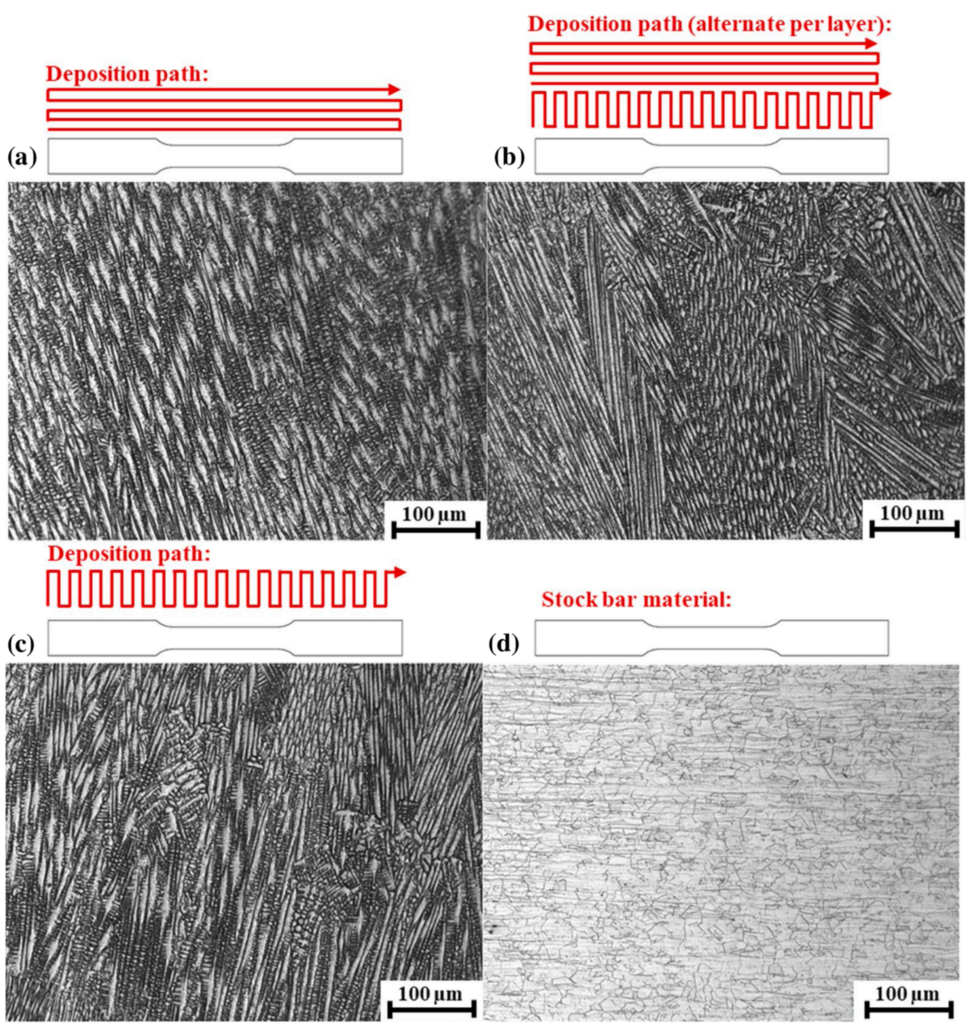

Fig. 13. Optical micrographs of microstructure for four experimental test specimen conditions (a) long unidirectional raster scan, (b) bidirectional raster scan, (c) short unidirectional raster scan build strategies and (d) stock bar material.

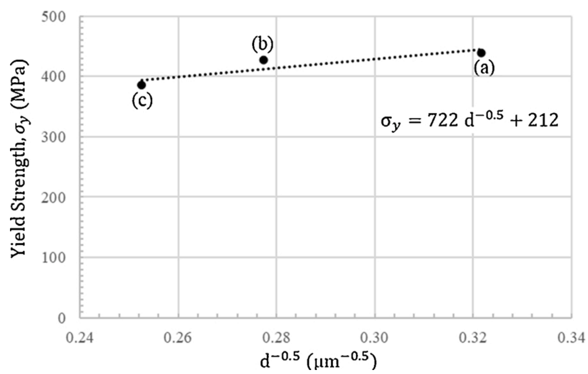

Fig. 14. Hall-Petch plot correlation between $d^{-0.5}$, where d is the measured grain size, and experimental yield strength results for four experimental test specimen conditions (a) long unidirectional raster scan, (b) bidirectional raster scan, (c) short unidirectional raster scan build strategies.

preferential in their orientation in the vertically oriented direction from the substrate. This type of grain growth is a result of the thermal history of the LMD process, resulting from heat flows through previously deposited layers and the substrate. The LMD process induced thermal gradients produces a non-steady-state solidification process with remelting and preferential metallurgical coarsening. In a previous study, it was found that the rapid cooling rates during the LMD process result in the retention of δ-ferritic phases that strengthens the austenitic matrix (Pang, Kaminski et al. 2019). Similar observations in the microstructural evolution of δ-ferritic phases were reported for LMD Stainless Steel 316 L specimens by Akbari and Kovacevic (2018) using x-ray diffraction techniques.

Wang et al. (2016) reported the effects of LMD process parameters on microstructure and tensile properties whereby the microstructural grain growth at the heat affected zone (HAZ) was presented as a function of the initial temperature conditions and heat input conditions. In these models, the microstructural grain growth is diffusion controlled, driven by surface energy, and requires no nucleation. It is shown that a higher initial temperature leads to a larger microstructural grain growth. The initial temperature can be taken as either a pre-heat temperature or thermal cycles that are a consequence of LMD's multi-pass depositions in raster scan build patterns. The differences in inter-track intervals per build strategy are attributed to the different thermal histories that arise from their respective deposition track lengths and number of deposition tracks per layer. During the LMD process, the temperature at the initiation point of each consecutive short unidirectional raster scan path is higher due to the shorter length of each raster scan path and the heat generated from the previous deposition path, resulting in lower thermal gradient. The temperature at the initiation point of each long unidirectional raster scan path is lower due to its comparatively longer length of each raster scan path, resulting in a steeper thermal gradient.

Based on their respective thermal histories, the short unidirectional raster scan build strategy employed in this study would result in a larger grain size than the long unidirectional raster scan build strategy. This is verified from the grain size measurements as seen in Table 2, where the mean grain size is 15.7 ± 1.2 μm for the short unidirectional raster scan, 13.0 ± 0.8 μm for the bidirectional raster scan, and 9.7 ± 0.9 μm for the long unidirectional raster scan build strategies. The grain size measurement results are consistent with the Hall-Petch relationship, whereby the short unidirectional raster scan samples, which has the largest mean grain size, has resulted in the lowest yield strength. The inverse is true for the long unidirectional raster scan samples as seen in Fig. 12 (c).

During the solidification process, ferrite becomes unstable compared to austenite with decreasing temperature. While the austenitic dendrites grow, some of the heavier elements begin to segregate, resulting in differences in the elemental composition at the interdendritic zones. As the solidification process continues, the remaining molten material retains ferrite stabilizing elements that favours the formation of δ-ferrite at the interdendritic areas (Takalo, Suutala et al. 1979). The higher the Cr_{eq}/Ni_{eq} ratio, the lower the starting temperature of the transformation in contrast to the liquidus temperature. A high Cr_{eq}/Ni_{eq} ratio produces a rapid cooling effect resulting in a Widmanstätten effect, where the growth of new phases occurs within the grain boundaries of the parent metal. This solidification effect produces a non-equiaxed grain morphology that increases the hardness and results in embrittlement of the material (Suutala, Takalo et al. 1980).

The ferrite concentration within the LMD-built part can be estimated using Schaeffler's diagram (Schaeffler, 1949) as seen in Fig. 15. The x-axis and the y-axis are the Cr equivalent and Ni equivalent respectively. The Cr equivalent is estimated from the wt. % of the ferrite stabilizing elements measured, and the Ni equivalent is estimated from the wt. % of the austenite stabilizing elements measured. The Cr equivalent and Ni equivalent equations are seen in Eq. (2) and (3). SEM images of the microstructure of each build strategy and the respective EDX area analysis locations are shown in Fig. 16. The measured elemental composition (wt. %) for each build strategy and the calculated Cr_{eq} and Ni_{eq} using Eq. (2) and (3) are compiled in Table 3.

$$\mathrm{Ni_{eq}} = \mathrm{Ni} + (30 \times \mathrm{C}) + (0.5 \times \mathrm{Mn}) \tag{2}$$

$$\mathrm{Cr_{eq}} = \mathrm{Cr} + \mathrm{Mo} + (1.5 \times \mathrm{Si}) + (0.5 \times \mathrm{Nb}) \tag{3}$$

The $\mathrm{Cr_{eq}/Ni_{eq}}$ ratio values of all three build strategies were found to be within the range of 1.56 to 1.67. This places all three build strategy specimens to be on the lower end of the ferritic-austenitic solidification mode region, where a duplex austenite and δ-ferrite microstructural composition is expected. This is in agreement with the results of the Schaeffler's diagram for the LMD-built SS316 L samples where a volumetric fraction of approximately 5% δ-ferrite was measured. The $\mathrm{Cr_{eq}/Ni_{eq}}$ ratio values were measured to be in a descending order from long unidirectional, to bidirectional, to short unidirectional raster scan build strategies. Since a higher $\mathrm{Cr_{eq}/Ni_{eq}}$ ratio produces an embrittlement and hardening effect due to its differences in solidification, the trend in the $\mathrm{Cr_{eq}/Ni_{eq}}$ ratios between each build strategy suggests that the long unidirectional raster scan has a higher hardness property, followed by bidirectional and short unidirectional raster scan build strategies respectively. By applying Tabor's model for hardness of austenitic steels (Tabor, 1951), the $\mathrm{Cr_{eq}/Ni_{eq}}$ trend between each build strategy is consistent with the measured yield strength from Fig. 12, where long unidirectional raster scan build strategy exhibited the highest yield strength, followed by the bidirectional and short unidirectional raster scan build strategies respectively.

3.4. Fracture surface topology

The 3D depth-of-focus reconstruction and 2D extended depth-of-field images of the fracture surface topologies for each experimental test specimen conditions is shown in Fig. 17. The

The LMD specimens from Fig. 17 (a), (b), and (c) exhibited little cross-sectional area reduction and distinct brittle fracture cleavage lines. The acicular grain crystal morphologies in the LMD specimens induce a strengthening effect that is evident in the brittle mechanical property observed from the tensile tests and are consistent with the fracture surface topologies. Rahman et al. (2019) found that brittle fracture observed in DED-produced carbon steel can be attributed to its martensitic matrix, retained austenite and networks of metal carbides. The long unidirectional raster scan from Fig. 17 (a), exhibited an irregular, 45° fracture surface topology resembling a longitudinal anisotropic fracture effect. The short unidirectional scan condition, from Fig. 17 (c) exhibited a near-flat, highly regular 45° fracture surface topology resembling a transverse anisotropic fracture effect. The bidirectional raster scan condition from Fig. 17 (b), the fracture surface

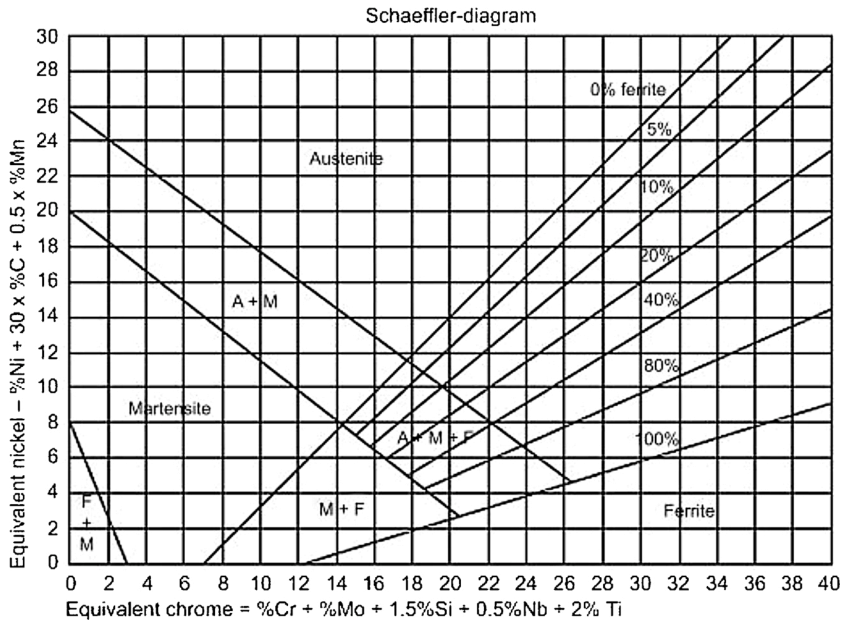

Fig. 15. Schaeffler diagram.

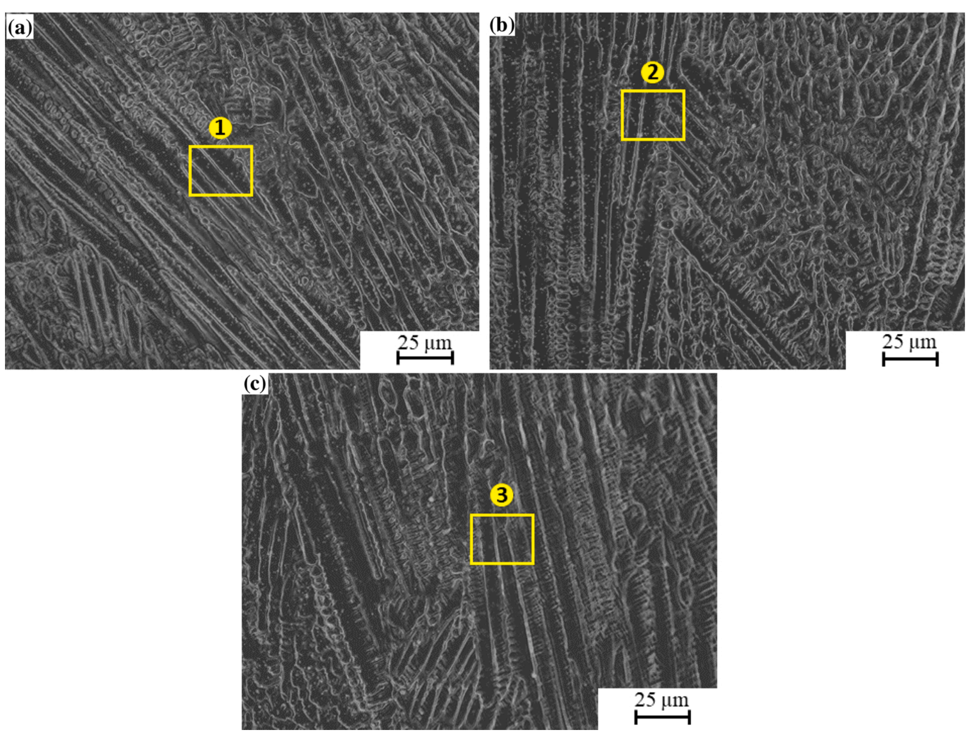

Fig. 16. SEM images and EDX area analysis locations for (a) long unidirectional raster scan, (b) bidirectional raster scan, and (c) short unidirectional raster scan.

Table 3
EDS measured composition (wt. %) of long unidirectional raster scan, bidirectional raster scan, and short unidirectional raster scan measurement areas indicated in boxes 1-3 respectively from Fig. 16, and Ni_{eq} and Cr_{eq}.

EDX area	C	Si	Cr	Mn	Ni	Mo	Fe	Cr_{eq}	Ni_{eq}	Cr_{eq}/Ni_{eq}
1	0.04	0.42	18.81	1.49	10.57	1.48	67.19	12.52	20.92	1.67
2	0.04	0.45	18.21	1.61	10.58	1.56	67.55	12.59	20.45	1.62
3	0.04	0.41	17.84	1.42	10.89	1.47	67.93	12.80	19.93	1.56

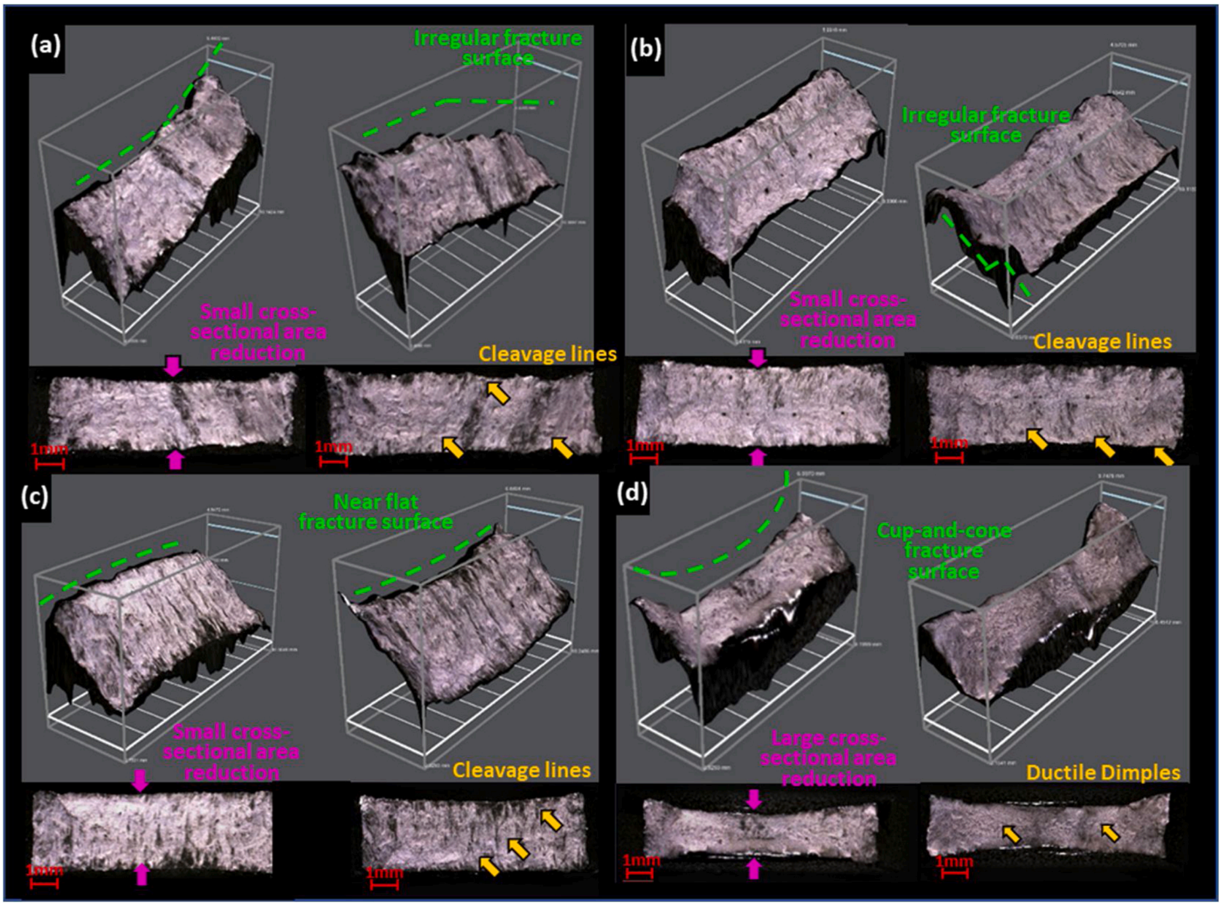

Fig. 17. Tensile specimen fracture surface topologies for the four experimental test specimen conditions (a) long unidirectional raster scan, (b) bidirectional raster scan, (c) short unidirectional raster scan, and (d) stock.

topology exhibited features that are a combination of that observed from the long and short unidirectional raster scan condition. The fracture surface topologies for the stock specimen condition shown in Fig. 17 (d) exhibited significant necking, with a typical ductile cup-and-cone topology, and multiple identifiable ductile dimples marked on the 2D extended depth-of-field images. These observations are consistent with the high degree of plastic strain measured from the tensile experiments, and the large grain crystal structures.

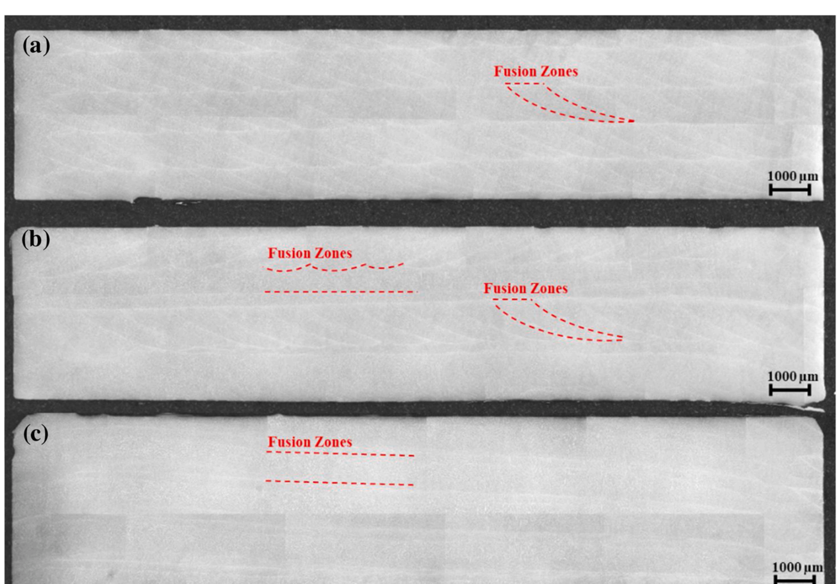

Fig. 18. Microscope images of etched cross-sections of LMD specimens for each build strategy (a) long unidirectional raster scan, (b) bidirectional raster scan, and (c) short unidirectional raster scan.

Chen et al. (2016) reported that laser additively manufactured parts are susceptible to liquation cracking at the fusion zone localities that propagate along the interdendritic region in the Heat Affected Zone (HAZ). Specific types of defects have the propensity to cluster between deposition layers due to the non-steady-state deposition process. Different arrays of deposition tracks within LMD components built with different build strategies play a role in contributing to the degree of anisotropy. To verify the role of the array of deposition track patterns on the mechanical anisotropy, a series of micro-indentation measurements was conducted at the fusion zone and deposition body locations.

3.5. Micro-indentation test

The section surface location for the micro-indentation measurements was illustrated earlier in Fig. 5. Images of the specimen's prepared etched surface were captured using a Zeiss Light Microscope and shown in Fig. 18. Micro-indentation tests were conducted to characterise the micro-hardness differences between the fusion zone region and deposition track body locations. Eight micro-indentation measurements were conducted in a line at the fusion zone and deposition track body locations each per specimen as shown in Fig. 19. Measurements were repeated on three LMD specimens, one per build strategy, and the result is summarized in Table 4.

From Table 4, the fusion zones exhibited higher hardness values than the deposition track body. The brittle characteristics of the fusion zones serve as fracture initiation sites during the tensile tests that result in the observed fracture surface topologies in Fig. 17, whereby a transverse and longitudinal anisotropic fracture effect were observed for the short and long unidirectional raster scan build strategies respectively. These findings are also consistent with the anisotropic behaviour in mechanical properties, like a lower UTS and yield strength for the short unidirectional than the long unidirectional raster scan build strategies seen from Fig. 12.

Yu et al. (2013) found that crack propagation tends to occur at the interdendritic regions of LMD Stainless Steel 316 L due to the differences in the material constitutions. Since, the array of fusion zones within the LMD builds are distributed differently for each build strategy, the mechanical properties would hence reflect this difference due to the fracture propagation that occurs across the different arrays of fusion zones as illustrated in Fig. 20.

4. Conclusion

In this study, the effects of Additive Manufacturing build strategies using LMD fabrication of Stainless Steel 316 L specimens provided a framework for characterizing the anisotropic properties and behaviour arising from build strategy pattern effects. In-situ process control was used to investigate the build strategy effects on the laser power control required to achieve consistent melt pool characteristics. A series of tensile tests were used to characterise the mechanical anisotropy of LMD specimens that were produced using long unidirectional, bidirectional, and short unidirectional raster scan build strategies. Mechanical anisotropy was established by correlating the LMD build process induced grain size effects to yield strength using the Hall-Petch relations. The δ-ferrite constituent of each sample was determined using Schaeffler diagram and Cr_{eq}/Ni_{eq} measurement methods. Micro-indentation hardness measurements show differences between the fusion zones and deposition track body locations showing the effects of build pattern on localized mechanical properties. The following conclusions can be made from this study:

Table 4
Micro-indentation measurements at deposition track body and fusion zone locations.

Location	Hardness (HV)
1 Deposition Track Body	221.4 ± 6.8
2 Fusion Line	255.4 ± 5.5

1 Different laser power regulation approaches are required to achieve consistent melt pool characteristics for different build strategies: short unidirectional, long unidirectional and bidirectional raster scans. Long unidirectional raster scan build strategy required ~8–10 % more energy input than the other build strategies in order to maintain a high degree of melt pool homogeneity.
2 Mechanical anisotropy was observed between different build strategies in the tensile tests results. The long unidirectional raster scan build strategy exhibited higher UTS, yield strength, fracture strain, but lower Young's modulus value than the bidirectional and short unidirectional raster scan build strategies respectively.
3 LMD specimens exhibited higher UTS, Young's modulus, yield strength, and lower fracture strain than conventionally manufactured stock bar specimens. This is due to the δ-ferritic phase, acicular crystal grain structures that are vertically oriented from the substrate in the LMD fabricated part. The stock bar specimens showed the typical austenitic grain structures giving ductile mechanical properties from the tensile test result.
4 The differences in thermal histories between the three build strategy raster scan patterns result in differences in the microstructural grain sizes, whereby the short unidirectional raster scan build strategy had larger grain size than the bidirectional and long unidirectional raster scan build strategies respectively. The Hall-Petch model result show anisotropy in yield strength with respect to the grain size arising from the different build strategy pattern effect.
5 The Cr_{eq}/Ni_{eq} ratio and the estimated δ-ferrite constituent for each build strategy was observed to be in a descending order from long unidirectional, bidirectional, and short unidirectional raster scan build strategies respectively, indicating a embrittlement and hardening effect for each build strategy in the same descending order.

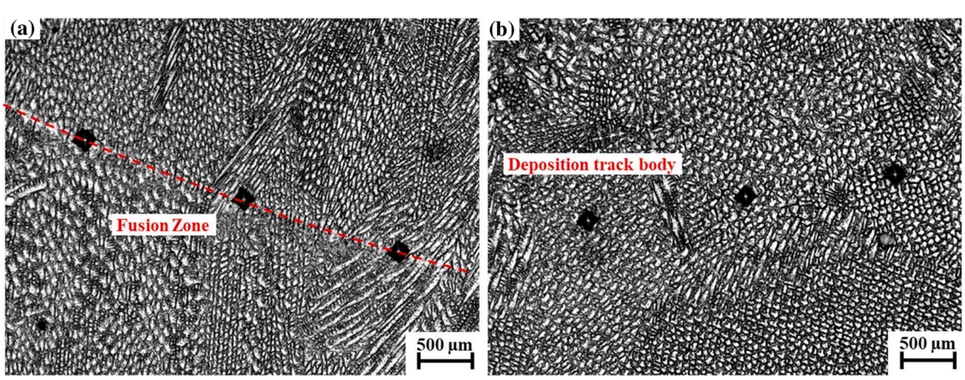

Fig. 19. Microscope images of micro-indentation sites at (a) fusion zone and (b) deposition track body locations.

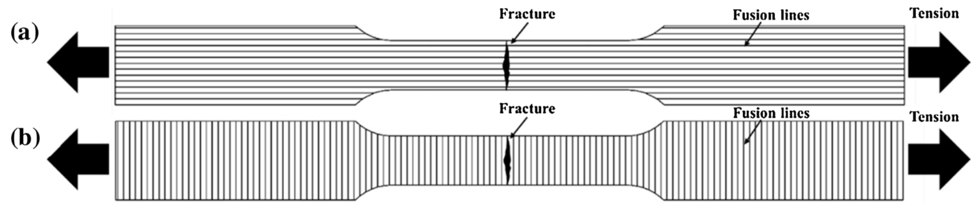

Fig. 20. Schematic of LMD tensile specimens under tension for (a) long unidirectional raster scan specimen undergoing longitudinal fracture effect and, (b) short unidirectional raster scan specimen undergoing transverse fracture effect.

6 The fracture surface topologies exhibited a transverse and longitudinal fracture effect in the short unidirectional and long unidirectional raster scans respectively. These fracture topology patterns from the tensile tests show that the arrays of deposition track patterns play a role in the eventual fracture mode.
7 Microindentation at the fusion zone and deposition track body locations show localized strengthening at the fusion zones. The arrays of fusion zones arising from the build strategy effects leads to differences in the distribution of localized strengthening across each sample.

CRediT authorship contribution statement

Eddie Tan Zhi'En: Conceived and designed the analysis; Collected the data; Contributed data or analysis tools; Performed the analysis; Wrote the paper. **John Hock Lye Pang:** Conceived and designed the analysis; Other contribution Oversaw and advised the research. **Jacek Kaminski:** Conceived and designed the analysis; Other contribution; Oversaw and advised the research

Declaration of Competing Interest

The authors declare that they have no conflicts of interest in preparing this manuscript. This manuscript has not been published and is not under review for publication elsewhere.

Acknowledgements

The first author would like to acknowledge the PhD scholarship from the Nanyang Technological University (NTU) and the support for the experimental work performed at the Advanced Remanufacturing and Technology Centre (ARTC).

References

Akbari, M., Kovacevic, R., 2018. An investigation on mechanical and microstructural properties of 316LSi parts fabricated by a robotized laser/wire direct metal deposition system. Addit. Manuf. 23, 487–497.
Amine, T., Newkirk, J.W., Liou, F., 2014. An investigation of the effect of direct metal deposition parameters on the characteristics of the deposited layers. Case Stud. Therm. Eng. 3, 21–34.
ASTM, 2014. "E112-113." Standard Test Methods for Determining Average Grain Size.
ASTM, 2016a. "E8 / E8M - 16a." Standard Test Methods for Tension Testing of Metallic Materials..
ASTM, 2016b. "E384-17." Standard Test Method for Knoop and Vickers Hardness of Materials..
ASTM, 2017. "A276 / A276M - 17 " Standard Specification for Stainless Steel Bars and Shapes.
Chen, Y., Zhang, K., Huang, J., Hosseini, S.R.E., Li, Z., 2016. Characterization of heat affected zone liquation cracking in laser additive manufacturing of Inconel 718. Mater. Des. 90, 586–594.
Donadello, S., Motta, M., Demir, A.G., Previtali, B., 2018. Coaxial laser triangulation for height monitoring in laser metal deposition. Procedia Cirp 74, 144–148.
Erfanmanesh, M., Abdollah-Pour, H., Mohammadian-Semnani, H., Shoja-Razavi, R., 2017. An empirical-statistical model for laser cladding of WC-12Co powder on AISI 321 stainless steel. Opt. Laser Technol. 97, 180–186.
Farahmand, P., Kovacevic, R., 2014. An experimental–numerical investigation of heat distribution and stress field in single-and multi-track laser cladding by a high-power direct diode laser. Opt. Laser Technol. 63, 154–168.
Forien, J.-B., Calta, N.P., DePond, P.J., Guss, G.M., Roehling, T.T., Matthews, M.J., 2020. Detecting keyhole pore defects and monitoring process signatures during laser powder bed fusion: a correlation between in situ pyrometry and ex situ X-ray radiography. Addit. Manuf., 101336
Goldak, J., Chakravarti, A., Bibby, M., 1984. A new finite element model for welding heat sources. Metall. Trans. B 15 (2), 299–305.
Hansen, N., 2004. Hall–Petch relation and boundary strengthening. Scr. Mater. 51 (8), 801–806.
Huang, Y., Ansari, M., Asgari, H., Farshidianfar, M.H., Sarker, D., Khamesee, M.B., Toyserkani, E., 2019. Rapid prediction of real-time thermal characteristics, solidification parameters and microstructure in laser directed energy deposition (powder-fed additive manufacturing). J. Mater. Process. Technol. 274, 116286.
Kashyap, B., Tangri, K., 1995. On the Hall-Petch relationship and substructural evolution in type 316L stainless steel. Acta Metall. Mater. 43 (11), 3971–3981.
Kisielewicz, A., Sikström, F., Christiansson, A.-K., Ancona, A., 2018. Spectroscopic monitoring of laser blown powder directed energy deposition of Alloy 718. Procedia Manuf. 25, 418–425.
Pang, J.H.L., Kaminski, J., Pepin, H., 2019. Characterisation of porosity, density, and microstructure of directed energy deposited stainless steel AISI 316L. Addit. Manuf. 25, 286–296.
Rahman, Ur, Capuano, N.L., Cabeza, S., Feinaeugle, M., Garcia-Junceda, A., de Rooij, M. B., Matthews, D.T.A., Walmag, G., Gibson, I., Römer, G.R.B.E., 2019. Directed energy deposition and characterization of high-carbon high speed steels. Addit. Manuf. 30, 100838.
Schaeffler, A.L., 1949. Constitution diagram for stainless steel weld metal. Metal progress 56 (11), 680.
Shi, Y., Li, Y., Liu, J., Yuan, Z., 2018. Investigation on the parameter optimization and performance of laser cladding a gradient composite coating by a mixed powder of Co50 and Ni/WC on 20CrMnTi low carbon alloy steel. Opt. Laser Technol. 99, 256–270.
Su, Y., Chen, B., Tan, C., Song, X., Feng, J., 2020. Influence of composition gradient variation on the microstructure and mechanical properties of 316 L/Inconel718 functionally graded material fabricated by laser additive manufacturing. J. Mater. Process. Technol., 116702
Suutala, N., Takalo, T., Moisio, T., 1980. Ferritic-austenitic solidification mode in austenitic stainless steel welds. Metall. Trans. A 11 (5), 717–725.
Tabor, D., 1951. The hardness and strength of metals. J. Inst. Metals 79, 1.
Takalo, T., Suutala, N., Moisio, T., 1979. Austenitic solidification mode in austenitic stainless steel welds. Metall. Trans. A 10 (8), 1173–1181.
Tyralla, D., Seefeld, T., 2020. Advanced process Monitoring in Additive Manufacturing: in-process temperature field measurement for laser metal deposition and laser powder bed fusion processes. PhotonicsViews 17 (3), 60–63.
Wang, Z., Palmer, T.A., Beese, A.M., 2016. Effect of processing parameters on microstructure and tensile properties of austenitic stainless steel 304L made by directed energy deposition additive manufacturing. Acta Mater. 110, 226–235.
Yu, J., Xin, L., Ma, Liang, Wang, Junjie, Fu, Xingling, Chen, Jing, Huang, Weidong, 2011. Influence of laser deposition patterns on part distortion, interior quality and mechanical properties by laser solid forming (LSF). Mater. Sci. Eng. A 528 (3), 1094–1104.
Yu, J., Rombouts, M., Maes, G., 2013. Cracking behavior and mechanical properties of austenitic stainless steel parts produced by laser metal deposition. Mater. Des. 45, 228–235.
Zhang, K., Wang, S., Liu, W., Shang, X., 2014. Characterization of stainless steel parts by laser metal deposition shaping. Mater. Des. 55, 104–119.